



The structure dependent electrochemical performance of porous Co_3O_4 nanoplates as anode materials for lithium-ion batteries



Congcong Liang, Danfei Cheng, Shujiang Ding, Pengfei Zhao, Mingshu Zhao, Xiaoping Song, Fei Wang*

MOE Key Laboratory for Nonequilibrium Synthesis and Modulation of Condensed Matter, School of Science, Xi'an Jiaotong University, Xi'an 710049, PR China

HIGHLIGHTS

- The structural and morphology of Co_3O_4 can be controlled by heating temperature.
- The structure of Co_3O_4 has considerable effect to their electrochemical performances.
- The robust single-crystal Co_3O_4 nanoplates exhibit excellent Li-storage performances.

ARTICLE INFO

Article history:

Received 22 August 2013

Received in revised form

9 November 2013

Accepted 27 November 2013

Available online 7 December 2013

Keywords:

Cobalt oxide

Nanoplate

Porous

Anode

Lithium-ion battery

ABSTRACT

The hexagon single-crystal $\text{Co}(\text{OH})_2$ nanoplates, which obtained by hydrothermal synthesis method, can be transformed to the porous single-crystal Co_3O_4 nanoplates after the heat treatment above 300°C in air. Electrochemical tests show that the lithium storage performances of porous Co_3O_4 nanoplates are influenced more closely to its structural aspects than its morphology and size factors, which can be controlled by changing the heat treatment temperature. When the heat treatment temperature is increased to 500°C , the robust single-crystal Co_3O_4 nanoplates with relatively large mesoporous size and low specific surface area can be obtained via the long-range atom diffusion at high temperature, which exhibit low initial irreversible capacity, superior cycling performance and excellent rate capability.

© 2013 Elsevier B.V. All rights reserved.

1. Introduction

As an important p-type semiconductor, nanostructured cobalt oxide (Co_3O_4) has been extensively studied due to its potential applications in catalysts, gas sensors, solar energy absorbers, field emission devices, magnetic materials and electrochemical capacitors, etc. [1–9]. More importantly, nano-sized Co_3O_4 is also regarded as an alternative anode material for lithium-ion batteries (LIBs) due to its high theoretical capacity (890 mAh g^{-1}) [10]. Nevertheless, the large initial irreversible capacities and poor cyclability over extended cycling are main problems for its application in practical LIBs. To improve the cycling performance of high capacity anode materials, intensive researches have been devoted to design and synthesis of loose, porous and hollow structure with small particle

size and high specific surface area, which is beneficial for accommodating the strain associated with severe volume variations during lithiation/delithiation processes [11–25]. Furthermore, nanocomposites based on the active/inactive concept is another effective approach to improve the cycling performance of high capacity anode materials. Thereinto, carbon materials are largely used as the inactive buffer material due to its soft nature and good electronic conductivity [26–34].

Whereas, the methods mentioned above usually result in large initial irreversible capacities due to their small particle size, high specific surface area and additional carbon contents, which might lead to more side reactions such as reductive decomposition of the electrolyte and formation of a solid electrolyte interface (SEI) layer [35]. Therefore, it's significant and also a great challenge to obtain both improved cyclability and reduced initial irreversible capacities. Among numerous research works, some Co_3O_4 nanomaterials with single-crystal structure and porous morphology should be the potential approaches to the problem. For example, the mesoporous

* Corresponding author. Tel.: +86 29 82663034; fax: +86 29 82665995.

E-mail address: feiwang@mail.xjtu.edu.cn (F. Wang).

single-crystal Co_3O_4 nano-needles [14] and nanoplates [24] exhibit both excellent cycling performance and low initial irreversible capacities. The robust single-crystal structure as well as porous morphology is beneficial to improve the cycling performance. The relatively large size and low specific surface area of the single-crystal materials can reduce the initial irreversible capacities. Furthermore, their special surface texture are also beneficial for electrode kinetics [11].

In this paper, we describe a large-scale solution routes for synthesis of hexagon and single-crystal $\text{Co}(\text{OH})_2$ nanoplates, which can be transformed to the porous and single-crystal Co_3O_4 nanoplates after the heat treatment above 300°C in air. 1,2-Propanediol is used as the organic solvent due to its relatively high viscosity, which should reduce the ion diffusion velocity in the solution and thus slow down the crystal growth process, which should be beneficial to reduce the size of the nanoplates and obtain single-crystal $\beta\text{-Co}(\text{OH})_2$. The morphology and structure of the Co_3O_4 nanoplates are strongly dependent on the heat treatment temperature, and have considerable effect to the electrochemical properties. When the heat treatment temperature is increased to 500°C , the obtained mesoporous and robust single-crystal Co_3O_4 nanoplates exhibit low initial irreversible capacity, superior cycling performance and excellent rate capability.

2. Experimental

In a typical synthesis, 0.3 mmol $\text{Co}(\text{CH}_3\text{COO})_2 \cdot 4\text{H}_2\text{O}$ was dissolved in a mixed solvent of 10 ml H_2O and 10 ml 1,2-Propanediol. Then, 10 ml of 1 M NaOH aqueous solution was added in above solution. After stirring at room temperature for 30 min, the resulting reaction mixture was transferred into a 50 ml Teflon-lined autoclave. The autoclave was sealed and maintained at 180°C for 24 h and then cooled down to room temperature naturally. The precipitates were separate by centrifugation and washed with distilled water and absolute ethanol several times. The obtained precipitates were dried

in a vacuum oven for 3 h at 60°C . Finally, the dried powders were heat-treated in air for 3 h at different temperatures.

The structure and morphology of the products were characterized by X-ray diffraction (XRD, Bruker D8-Advance, $\text{Cu-K}\alpha$, $\lambda = 0.15406\text{ nm}$), field emission scanning electron microscope (FESEM, JEOL JSM-7100F) and transmission electron microscopy (TEM, JEOL JEM-2100). The nitrogen adsorption–desorption isotherms were measured using Micromeritics ASAP 2020M gas sorption system. BET and BJH methods were introduced to calculate surface area and pore size distribution.

Electrochemical properties of Co_3O_4 electrodes were tested using two-electrode Swagelok cells with lithium metal as the counter and reference electrodes. The working electrodes consisted of 70 wt.% active materials (Co_3O_4), 20 wt.% conductive materials (acetylene black), and 10 wt.% binder (polyvinylidene fluoride, PVDF). The electrolyte was 1 M LiPF_6 in a mixture of 50 vol.% ethylene carbonate (EC) and 50 vol.% diethylene carbonate (DEC). Test cells were assembled in argon filled glove box. The charge–discharge measurements were carried out on Arbin BT2000 battery testing system in the voltage range of 0.02 V–3.0 V (vs. Li/Li^+).

3. Results and discussion

Large-scale hexagonal nanoplates were obtained by using a solvothermal method (Fig. 1a). The XRD pattern of the obtained product is shown in the insert pattern of Fig. 1a. All of the diffraction peaks can be indexed as hexagonal $\beta\text{-Co}(\text{OH})_2$, which is in agreement with the literature values (JCPDS No. 30-0443). No impurity peaks were detected, revealing the high purity of the synthesized products. Fig. 1b and c shows the FESEM and TEM images of $\beta\text{-Co}(\text{OH})_2$ nanoplates, which illustrate that the sample displays a hexagonal plate-like morphology with width of several hundred nanometers and typical thickness in the range of 30–40 nm. Fig. 1d and e shows a representative TEM image of an individual nanoplate and corresponding selected-area electron diffraction (SAED)

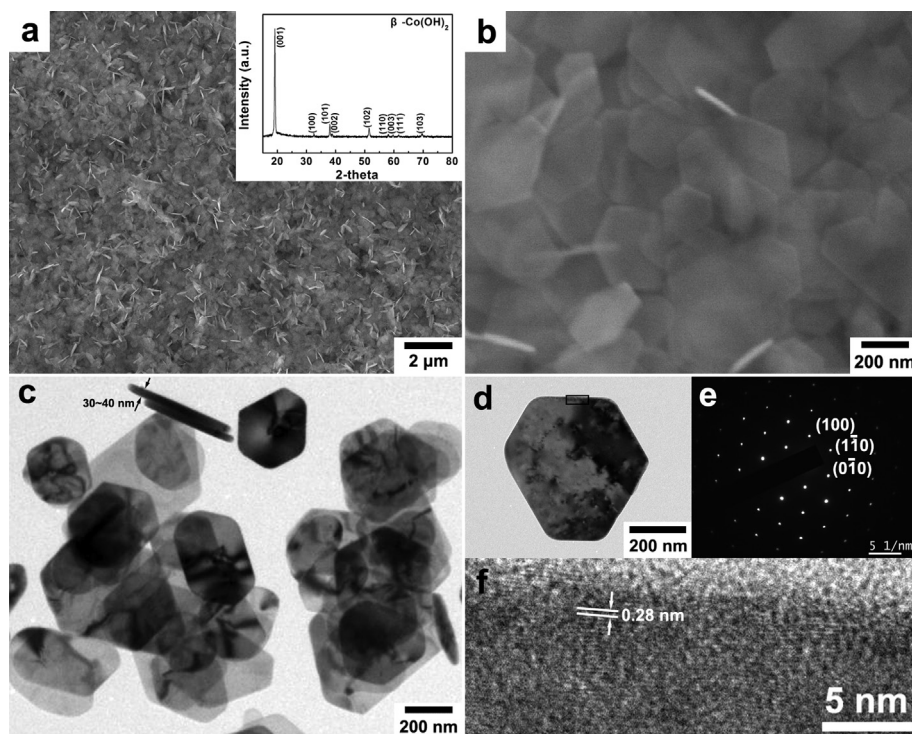


Fig. 1. (a, b) SEM images of the $\beta\text{-Co}(\text{OH})_2$ nanoplates; (c) TEM image of the $\beta\text{-Co}(\text{OH})_2$ nanoplates; (d) TEM image of an individual $\beta\text{-Co}(\text{OH})_2$ nanoplate; (e) SAED pattern of (d); (f) HRTEM image of the selected black rectangle in (d). The inset in (a) is the XRD pattern of $\beta\text{-Co}(\text{OH})_2$ nanoplates.

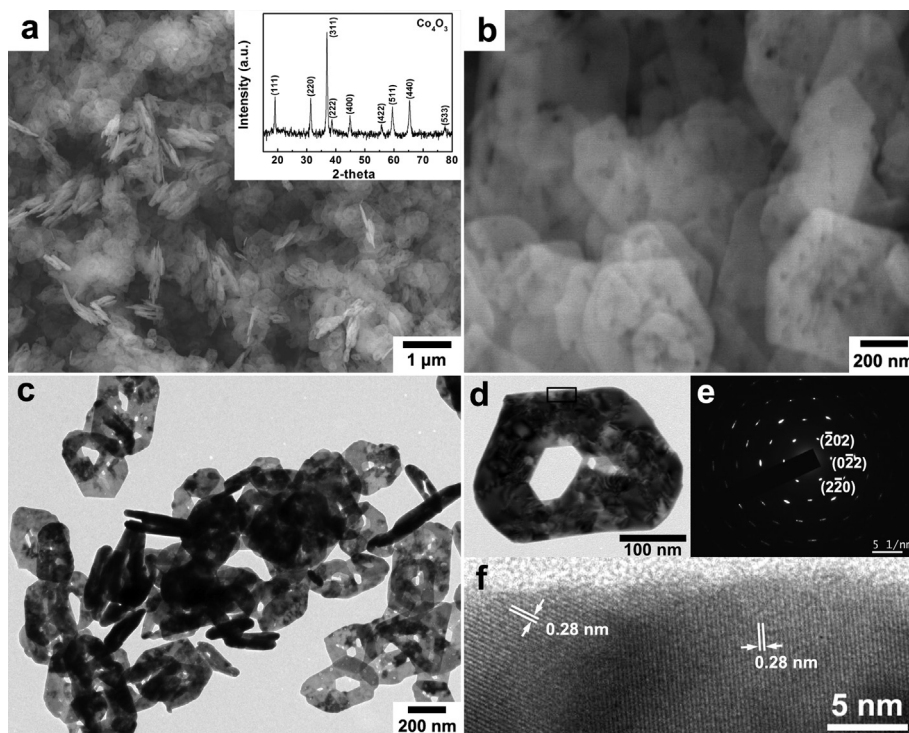


Fig. 2. (a, b) SEM images of the Co_3O_4 nanoplates; (c) TEM image of the Co_3O_4 nanoplates; (d) TEM image of an individual Co_3O_4 nanoplate; (e) SAED pattern of (d); (f) HRTEM image of the selected black rectangle in (d). The sample is heat treated at 500°C , the inset in (a) is the XRD pattern of Co_3O_4 nanoplates.

pattern with zone axis $[001]$. The SAED pattern reveals a typical single-crystalline nature and all diffraction spots in it can be indexed to the hexagonal $\beta\text{-Co}(\text{OH})_2$, which is in agreement with the powder XRD result. Fig. 1f shows the high-resolution TEM

(HRTEM) image of the selected black rectangle in Fig. 1d, which reveals fringes perpendicular to the nanoplate. The measured lattice spacing is 0.28 nm , corresponding to the interlayer spacing of the (100) planes of $\beta\text{-Co}(\text{OH})_2$ ($d = 0.2755\text{ nm}$).

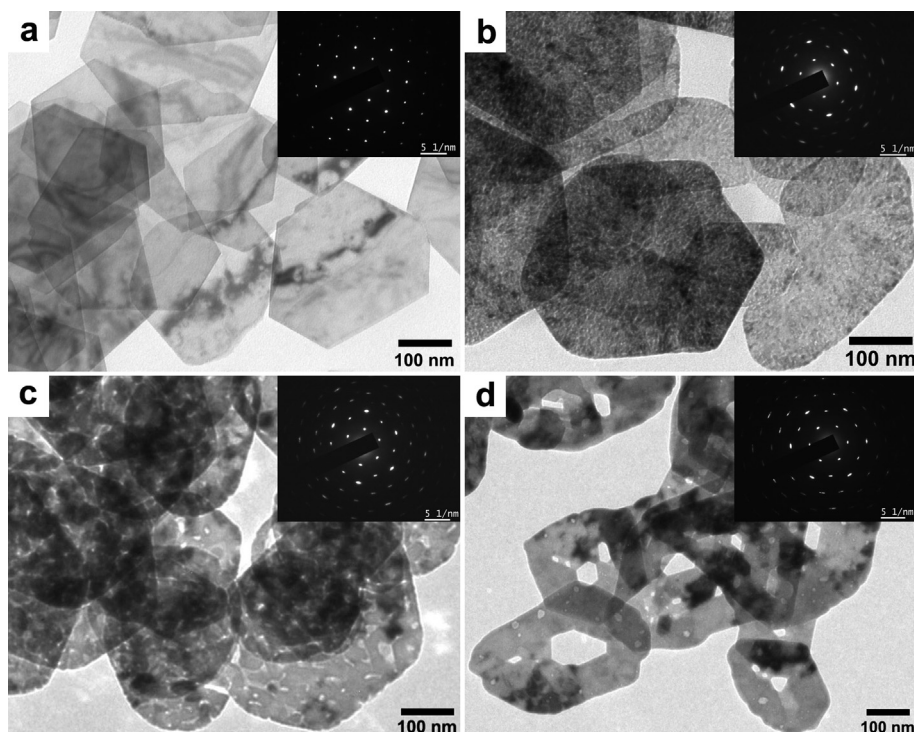


Fig. 3. TEM image of the precursor $\beta\text{-Co}(\text{OH})_2$ nanoplates (a); TEM images of the Co_3O_4 nanoplates heat treated at 300°C (b), 400°C (c) and 500°C (d). The insets in TEM images are the corresponding SAED patterns.

The insert pattern of Fig. 2a shows the XRD analysis of the sample prepared by heat-treating the precursor β -Co(OH)₂ nanoplates in air at 500 °C. All diffraction peaks in it can be perfectly indexed to cubic spinel Co₃O₄ (JCPDS No. 42-1467). Fig. 2a and b shows low- and high-magnification FESEM images of Co₃O₄ nanoplates, respectively. From Fig. 2b, it can be observed that the hexagonal plate-like morphology of precursor β -Co(OH)₂ is retained during the thermal conversion, while the pores are formed inside Co₃O₄ nanoplates due to the dehydration and crystalline structure transformation during thermal treatment. The porous characteristic of Co₃O₄ nanoplates is showed more clearly in the TEM image (Fig. 2c). To further investigate the microstructures of Co₃O₄ nanosheets, Fig. 2d–f shows a typical porous Co₃O₄ nanoplate as well as its SAED pattern and HRTEM image. Different from the conventional small pores formed uniformly in the matrix, one large pore forms in the middle of the nanoplate at this condition. The corresponding SAED pattern (Fig. 2e) shows that the nanoplate is a single-crystalline structure. All diffraction spots in it can be indexed to cubic spinel Co₃O₄. The single-crystalline nature is also confirmed by HRTEM image (Fig. 2f), in which all crystal lattices have the same crystallographic orientation. The lattice fringes show an interplanar spacing of about 0.28 nm, corresponding to the (220) plane of the cubic Co₃O₄ ($d = 0.2858$ nm).

It is well known that the β -Co(OH)₂ is thermally unstable. It can be converted into stable spinel-type Co₃O₄ at a temperature below 200 °C. The formation of Co₃O₄ is due to the oxidation and dehydration of Co(OH)₂ during thermal treatment process ($6\text{Co(OH)}_2 + \text{O}_2 \rightarrow 2\text{Co}_3\text{O}_4 + 6\text{H}_2\text{O}$). In this process, the temperature plays an important role, which can markedly influence the morphology characteristic, crystal structure and structure stability of the products. Fig. 3 shows the morphology and structure changes of β -Co(OH)₂ heat-treated at different temperatures. The insert SAED patterns of Fig. 3b–d show that the crystal structure is completely transformed to cubic Co₃O₄ when the heating temperature exceeds 300 °C for 3 h. However, the morphologies are quite different between them. Comparing with the precursor β -Co(OH)₂, there are numerous tiny pores formed and spread all over the nanoplates after the heat treatment at 300 °C, as shown in Fig. 3b. In this stage, the atom diffusion is limited due to the relatively low heating temperature. As a result, only tiny pores can be formed because the structural rearrangement is restricted in small area. Elevating the heating temperature to 400 °C (Fig. 3c), the pore size is obviously increased due to the improvement of the atom diffusion ability. The effect of the temperature is more prominent when it is further elevated to 500 °C. In this moment, the pore size and distribution undergoes considerable changes. Pore size reaches to tens of nanometers and some larger center pores formed instead of the uniform distribution of smaller pore (Fig. 3d). Meanwhile, the nanoplates have an obvious shrinkage, which should result in more stable structure.

The specific surface area and BJH pore size distribution of Co₃O₄ also have obvious changes at different heat treatment temperatures, which were obtained based on the nitrogen adsorption–desorption isotherms carried out at 77 K. From Fig. 4a we can see that the Co₃O₄ nanoplates heat treated at 300 °C have a narrow pore size distribution and the pore size is focused on about 3.6 nm (peak value). Increasing the heat treatment temperature to 400 °C, the pore size has an obvious increasing to about 6.7 nm (peak value) and the pore size distribution changes to a relatively broad range, as shown in Fig. 4b. Further increasing the heat treatment temperature to 500 °C, some extremely large pores are formed and the pore size distribution becomes irregular, which can't be real reflected by BJH pore size distribution and also don't display here. All results of BJH pore size distribution are well consistent with the TEM characterizations. Furthermore, the specific surface area of Co₃O₄ also shows regular

changes at different heat treatment temperatures. With the increasing of heat treatment temperature, both the crystallite size and the pore size increase obviously, which lead to the reducing of the specific surface area. From Fig. 4 we can see that the specific surface areas of Co₃O₄ heat treated at 300 °C, 400 °C and 500 °C are 86.18 m² g^{−1}, 28.43 m² g^{−1} and 14.53 m² g^{−1}, respectively.

Fig. 5a illustrates the voltage–capacity curves (0.2 C, 1 C = 890 mAh g^{−1}) of the Co₃O₄ nanoplates heat treated at 500 °C. During the first discharge process, the voltage curve includes a long plateau at about 1.0 V and a continuous voltage slope down to 0.02 V. The voltage plateau corresponds to the reversible Li-driven

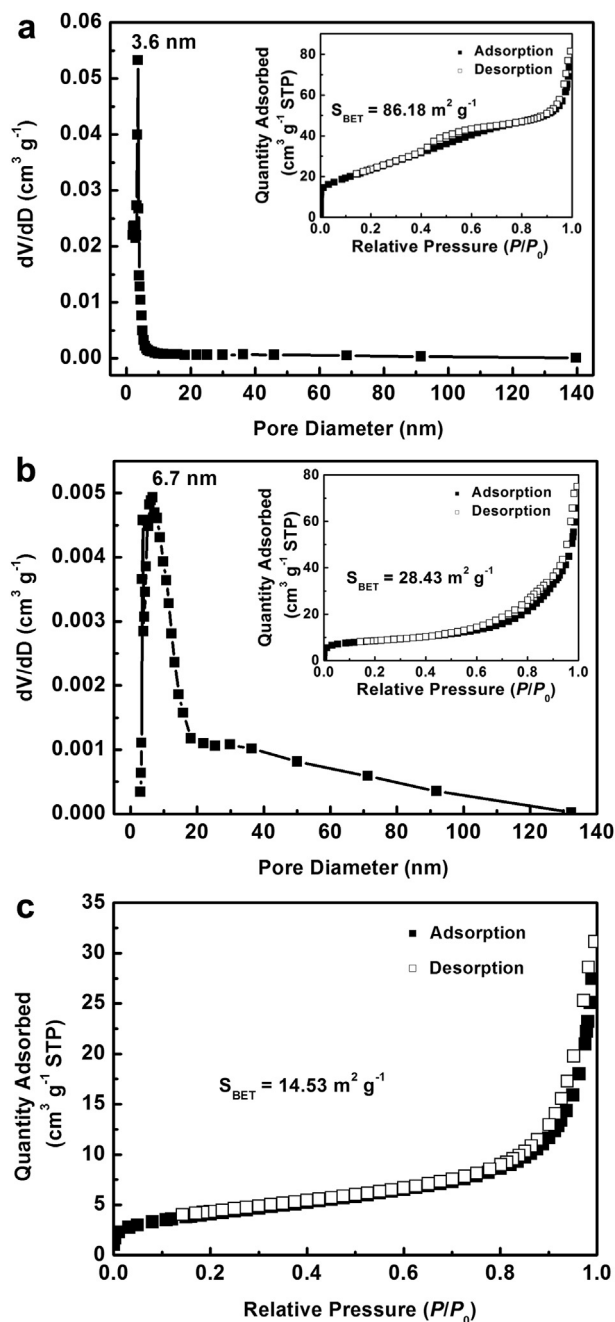


Fig. 4. (a) The pore size distribution of the Co₃O₄ nanoplates heat treated at 300 °C (the inset is the corresponding adsorption–desorption isotherms); (b) the pore size distribution of the Co₃O₄ nanoplates heat treated at 400 °C (the inset is the corresponding adsorption–desorption isotherms); (c) the adsorption–desorption isotherms of the Co₃O₄ nanoplates heat treated at 500 °C.

decomposition of Co_3O_4 as well as the irreversible formation of a SEI layer [35]. The voltage slope should be associated with the reversible formation/dissolution of a gel-like film on the surface of oxide particles, which can lead to an extra reversible capacity besides the reversible reaction mechanism ($\text{Co}_3\text{O}_4 + 8\text{Li}^+ + 8\text{e}^- \leftrightarrow 4\text{Li}_2\text{O} + 3\text{Co}$) [36,37]. Therefore, the actual reversible capacity of Co_3O_4 usually exceeds its theoretical values [14,15]. During the first charge process, the voltage plateau at about 2.0 V should be ascribed to the reversible oxidation of Co to cobalt oxide. In the following cycles, the voltage–capacity curves exhibit highly consistent, which demonstrate superior cycle stability of the Co_3O_4 nanoplates during the lithiation/delithiation processes.

Fig. 5b shows the cycling performance and coulomb efficiency of the Co_3O_4 nanoplates heat treated at 500 °C. The initial discharge and charge capacities are 1461 mAh g^{-1} and 1070 mAh g^{-1} , respectively. The initial irreversible capacities are mainly ascribed to the decomposition of the electrolyte and the formation of the SEI layer, which are significantly influenced by the specific surface area of the electrode materials. Due to the relatively low specific surface area, the coulomb efficiency of the Co_3O_4 nanoplates in the first cycle is up to 73.3%. Thereafter, the coulomb efficiencies are increased gradually and stabilized above 98% after 8 cycles. Except the first cycle, no obvious capacity fade is found within 80 cycles and the discharge capacity at 80th cycle can be maintained at 1001 mAh g^{-1} . The excellent cycling performance of the Co_3O_4 nanoplates should be attributed to its 2D porous morphology and robust single-crystal structure. The 2D porous morphology can provide short ion/electron diffusion path and also be beneficial for accommodating the strain induced by the severe volume variations during Li^+ insertion and extraction. And the robust single-crystal structure can provide strong structural stability during the charge/discharge processes, which should be more important to obtain superior long-term cycling performance.

The rate capability of the Co_3O_4 nanoplates heat treated at 500 °C is shown in Fig. 5c. From it we can see that the capacity of about 1000 mAh g^{-1} is obtained at 0.2 C after 10 cycles and this value can be maintained at 0.5 C and 1 C. When the current density is further improved to 2 C, the capacity has a slight reducing and

reach to 893 mAh g^{-1} at 40th cycle. Furthermore, the capacity can increase to about 1150 mAh g^{-1} when the current density turns back to 0.2 C. The gradual increase of the capacity should be attributed that the polymer layer on the internal surface of the Co_3O_4 nanoplates builds-up slowly, over a number of cycles [12,37]. The excellent rate capability indicates a fast transferring of electrons and Li^+ in 2D porous Co_3O_4 nanoplates because of their large electrode-electrolyte contact area and short Li^+ diffusion distance. More importantly, the robust single-crystalline structure may also be propitious to the charge transfer during lithiation/delithiation processes because less crystallite boundaries present in them and their special surface texture are also beneficial for electrode kinetics [11,24].

Fig. 5d compares the cycling performance of Co_3O_4 nanoplates heat treated at 300 °C, 400 °C and 500 °C. From the morphology characterizations we can see that the main differences between them are pore size and specific surface area. Considering the effect of them, the sample heat treated at lower temperature should have better cycling performance because the smaller size and larger specific surface area can provide larger electrolyte/electrode contact area and shorter ion/electron diffusion path. However, Fig. 5d indicates that the cycling performance deteriorates quickly with the decreasing of the heat treatment temperature. The results show that the electrochemical performance of Co_3O_4 nanoplates should be influenced more closely to its structural aspects than its morphology and size factors. Therefore, the Co_3O_4 nanoplates heat treated at 500 °C should have more robust single-crystal structure and thus provide stronger structure relationship and better structural stability during the lithiation/delithiation processes, which improves the capacity retention over prolonged discharge–charge cycles.

4. Conclusions

In summary, the hexagon single-crystal $\text{Co}(\text{OH})_2$ nanoplates can be transformed to the porous single-crystal Co_3O_4 nanoplates after the heat treatment above 300 °C in air. The heat treatment temperature has considerable effect to the morphology and structure of the Co_3O_4 nanoplates. Electrochemical tests show that the lithium

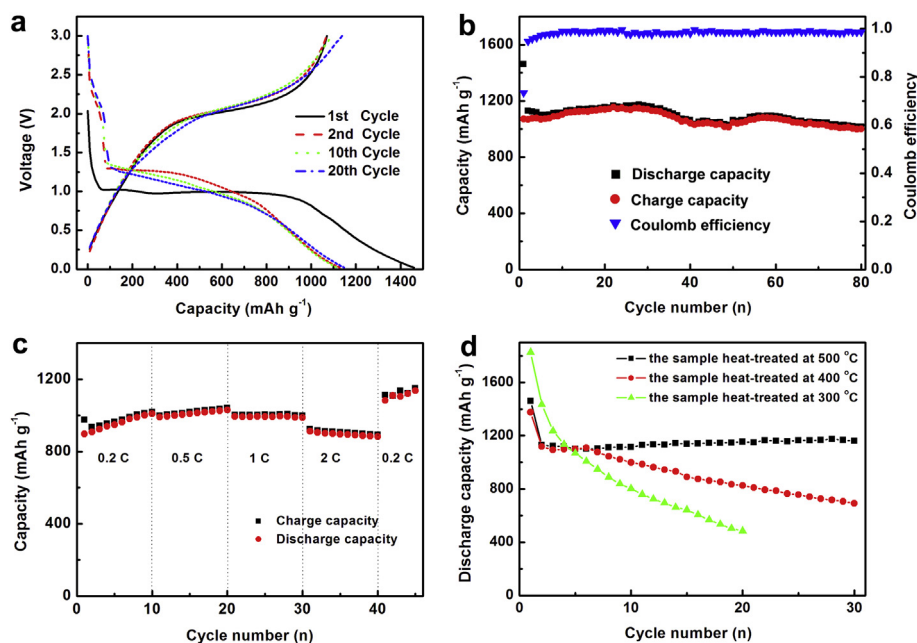


Fig. 5. (a) Voltage–capacity curves for different cycles of the Co_3O_4 nanoplates heat treated at 500 °C; (b) cycling performance of the Co_3O_4 nanoplates heat treated at 500 °C; (c) rate capability of the Co_3O_4 nanoplates heat treated at 500 °C; (d) cycling performance comparison of the Co_3O_4 nanoplates heat treated at different temperatures.

storage performances of porous Co_3O_4 nanoplates are influenced more closely to its structural aspects than its morphology and size factors. When the heat treatment temperature is increased to 500 °C, the robust single-crystal Co_3O_4 nanoplates with relatively large mesoporous size and low specific surface area exhibit low initial irreversible capacity, superior cycling performance and excellent rate capability. Considering the improved electrochemical performance and large scale synthesis, the obtained mesoporous Co_3O_4 nanoplates with robust single-crystal structure should be suitable as anode materials for high performance lithium-ion batteries.

Acknowledgments

This work was supported by National Natural Science Foundation of China (51002117), Specialized Research Fund for the Doctoral Program of Higher Education of China (20100201120049) and Fundamental Research Funds for the Central Universities.

References

- [1] W.Y. Li, L.N. Xu, J. Chen, *Adv. Funct. Mater.* 15 (2005) 851–857.
- [2] D. Patil, P. Patil, V. Subramanian, P.A. Joy, H.S. Potdar, *Talanta* 81 (2010) 37–43.
- [3] F. Jiao, H. Frei, *Angew. Chem. Int. Ed.* 48 (2009) 1841–1844.
- [4] C.Y. Ma, Z. Mu, J.J. Li, Y.G. Jin, J. Cheng, G.Q. Lu, Z.P. Hao, S.Z. Qiao, *J. Am. Chem. Soc.* 132 (2010) 2608–2613.
- [5] M. Ando, K. Kadono, K. Kamada, K. Ohta, *Thin Solid Films* 446 (2004) 271–276.
- [6] T. Yu, Y.W. Zhu, X.J. Xu, Z.X. Shen, P. Chen, C.T. Lim, J.T.L. Thong, C.H. Sow, *Adv. Mater.* 17 (2005) 1595–1599.
- [7] M.J. Benitez, O. Petravic, E.L. Salabas, F. Radu, H. Tüysüz, F. Schüth, H. Zabel, *Phys. Rev. Lett.* 101 (2008) 097026.
- [8] T. Zhu, J.S. Chen, X.W. Lou, *J. Mater. Chem.* 20 (2010) 7015–7020.
- [9] F. Zhang, C.Z. Yuan, X.J. Lu, L.J. Zhang, Q. Che, X.G. Zhang, *J. Power Sources* 203 (2012) 250–256.
- [10] P. Poizot, S. Laruelle, S. Grugeon, L. Dupont, J.-M. Tarascon, *Nature* 407 (2000) 496–499.
- [11] S.L. Xiong, J.S. Chen, X.W. Lou, H.C. Zeng, *Adv. Funct. Mater.* 22 (2012) 861–871.
- [12] K.M. Shaju, F. Jiao, A. Débart, P.G. Bruce, *Phys. Chem. Chem. Phys.* 9 (2007) 1837–1842.
- [13] X.W. Lou, D. Deng, J.Y. Lee, J. Feng, L.A. Archer, *Adv. Mater.* 20 (2008) 258–262.
- [14] X.W. Lou, D. Deng, J.Y. Lee, L.A. Archer, *J. Mater. Chem.* 18 (2008) 4397–4401.
- [15] F.M. Zhang, B.Y. Geng, Y.J. Guo, *Chem. Eur. J.* 15 (2009) 6169–6174.
- [16] L. Tian, H.L. Zou, J.X. Fu, X.F. Yang, Y. Wang, H.L. Guo, X.H. Fu, C.L. Liang, M.M. Wu, P.K. Shen, Q.M. Gao, *Adv. Funct. Mater.* 20 (2010) 617–623.
- [17] J. Liu, H. Xia, L. Lu, D.F. Xue, *J. Mater. Chem.* 20 (2010) 1506–1510.
- [18] J.S. Chen, T. Zhu, Q.H. Hu, J.J. Gao, F.B. Su, S.Z. Qiao, X.W. Lou, *ACS Appl. Mater. Interfaces* 2 (2010) 3628–3635.
- [19] Y.Q. Fan, H.B. Shao, J.M. Wang, L. Liu, J.Q. Zhang, C.N. Cao, *Chem. Commun.* 47 (2011) 3469–3471.
- [20] X.Y. Xue, S. Yuan, L.L. Xing, Z.H. Chen, B. He, Y.J. Chen, *Chem. Commun.* 47 (2011) 4718–4720.
- [21] X. Wang, H. Guan, S.M. Chen, H.Q. Li, T.Y. Zhai, D.M. Tang, Y. Bando, D. Golberg, *Chem. Commun.* 47 (2011) 12280–12282.
- [22] Y. Sun, X.Y. Feng, C.H. Chen, *J. Power Sources* 196 (2011) 784–787.
- [23] N. Yan, L. Hu, Y. Li, Y. Wang, H. Zhong, X.Y. Hu, X.K. Kong, Q.W. Chen, *J. Phys. Chem. C* 116 (2012) 7227–7235.
- [24] F. Wang, C.C. Lu, Y.F. Qin, C.C. Liang, M.S. Zhao, S.C. Yang, Z.B. Sun, X.P. Song, *J. Power Sources* 235 (2013) 67–73.
- [25] J.Y. Wang, N.L. Yang, H.J. Tang, Z.H. Dong, Q. Jin, M. Yang, D. Kisailus, H.J. Zhao, Z.Y. Tang, D. Wang, *Angew. Chem. Int. Ed.* 52 (2013) 6417–6420.
- [26] Z.S. Wu, W.C. Ren, L. Wen, L.B. Gao, J.P. Zhao, Z.P. Chen, G.M. Zhou, F. Li, H.M. Cheng, *ACS Nano* 4 (2010) 3187–3194.
- [27] L.Y. Pan, H.B. Zhao, W.C. Shen, X.W. Dong, J.Q. Xu, *J. Mater. Chem. A* 1 (2013) 7159–7166.
- [28] L.Q. Tao, J.T. Zai, K.X. Wang, H.J. Zhang, M. Xu, J. Shen, Y.Z. Su, X.F. Qian, *J. Power Sources* 202 (2012) 230–235.
- [29] J. Chen, X.H. Xia, J.P. Tu, Q.Q. Xiong, Y.X. Yu, X.L. Wang, C.D. Gu, *J. Mater. Chem.* 22 (2012) 15056–15061.
- [30] M.W. Xu, F. Wang, Y. Zhang, S. Yang, M.S. Zhao, X.P. Song, *Nanoscale* 5 (2013) 8067–8072.
- [31] G.P. Kim, I. Nam, N.D. Kim, J. Park, S. Park, J. Yi, *Electrochem. Commun.* 22 (2012) 93–96.
- [32] Q.Y. Han, J.T. Zai, Y.L. Xiao, B. Li, M. Xu, X.F. Qian, *RSC Adv.* 3 (2013) 20573–20578.
- [33] Y.L. Xiao, J.T. Zai, L.Q. Tao, B. Li, Q.Y. Han, C. Yu, X.F. Qian, *Phys. Chem. Phys.* 15 (2013) 3939–3945.
- [34] J.T. Zai, C. Yu, Q. Zou, L.Q. Tao, K.X. Wang, Q.Y. Han, B. Li, Y.L. Xiao, X.F. Qian, *RSC Adv.* 2 (2012) 4397–4403.
- [35] P. Poizot, S. Laruelle, S. Grugeon, L. Dupont, J.-M. Tarascon, *J. Power Sources* 97–98 (2001) 235–239.
- [36] S. Laruelle, S. Grugeon, P. Poizot, M. Dolle, L. Dupont, J.-M. Tarascon, *J. Electrochem. Soc.* 149 (2002) A627–A634.
- [37] F. Wang, W.Z. Tao, M.S. Zhao, M.W. Xu, S.C. Yang, Z.B. Sun, L.Q. Wang, X.P. Song, *J. Alloys Compd.* 509 (2011) 9798–9803.